Accepted Manuscript

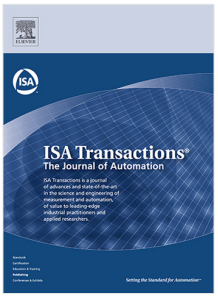

New hybrid sensorless speed of a non-salient pole PMSG coupled to wind turbine using a modified switching algorithm

Mansouri Mohamed, Hassaine Said, Larbi Mhamed, Bey Mohamed, Allaoui Tayeb, Denai Mouloud, Moudjahed Mohamed

PII: S0019-0578(19)30198-3
DOI: https://doi.org/10.1016/j.isatra.2019.04.024
Reference: ISATRA 3184

To appear in: *ISA Transactions*

Received date : 23 July 2018
Revised date : 17 April 2019
Accepted date : 24 April 2019

Please cite this article as: M. Mohamed, H. Said, L. Mhamed et al., New hybrid sensorless speed of a non-salient pole PMSG coupled to wind turbine using a modified switching algorithm. *ISA Transactions* (2019), https://doi.org/10.1016/j.isatra.2019.04.024

*Title page showing Author Details

New Hybrid Sensorless Speed of a Non-Salient Pole PMSG Coupled to Wind Turbine Using a Modified Switching Algorithm.

Author names:

Mansouri Mohamed[a], Hassaine Said[a], Larbi Mhamed[a], Bey Mohamed[a]. Allaoui Tayeb[a].

Denai Mouloud[b], Moudjahed Mohamed[a]

Author Emails:

Mohamed.mansouri@univ-tiaret.dz, s_hassaine@yahoo.fr larbi_mh@yahoo.fr, Mohamed.bey@univ-tiaret.dz allaoui_tb@yahoo.fr m.denai@herts.ac.uk moudjahedm@yahoo.fr

Author Affiliations:

[a] Laboratory of Energy Engineering and Computer Engineering, IBN Khaldoun University, Tiaret, Algeria.

[b] School of Engineering and Technology, University of Hertfordshire, Hatfield, UK

Highlights

- A new hybrid observer is proposed to estimate the position and speed of a non-salient pole PMSG driven by a wind turbine.
- The hybrid structure combines two observers and allow the system to operate safely over a wide speed range without losing control.
- The proposed switching algorithm between the two observers is based on the weighting coefficients method, which is characterized by simplicity and a low computation time.
- Speed control is based on fuzzy logic to provide robustness and performance at low speeds.
- The proposed hybrid observer and control scheme are implemented in Matlab/Simulink and several simulation scenarios are presented to demonstrate the performance of the wind power system.

New Hybrid Sensorless Speed of a Non-Salient Pole PMSG Coupled to Wind Turbine Using a Modified Switching Algorithm

Abstract

The paper focuses on the design of position and speed observers for the rotor of a non-salient pole permanent magnet synchronous generator (NSPPMSG) coupled to a wind turbine. With the random nature of wind speed this observer is required to provide a position and speed estimates over a wide speed range. The proposed hybrid structure combines two observers and a switching algorithm to select the appropriate observer based on a modified weighting coefficients method. The first observer is a higher order sliding mode observer (HOSMO) based on modified super twisting algorithm (STA) with correction term and operates in the medium and nominal wind speed ranges. The second observer is used in the low speed range and is based on the rotor flux estimation and the control by injecting a direct reference current different to zero. The stability of each observer has been successfully assessed using an appropriate Lapunov function. The simulation results obtained show the effectiveness and performance of the proposed observer and control scheme.

Keywords:

Non-salient PMSG, standalone wind turbine, high-order sliding mode, super-twisting algorithm, fuzzy logic control.

1. Introduction

Currently, wind energy is among the fastest growing renewable energy sources worldwide and wind power industry has experienced a rapid development over the last decade. Wind energy conversions systems (WECS) with various wind turbine configurations and generator types have been extensively studied and the doubly-fed induction generator (DFIG) and squirrel-cage induction generators (SCIG) have been the most commonly used generator

technologies. In recent years, variable-speed WECS based on permanent magnet synchronous generators (PMSG) are becoming increasingly popular because of their advantages such as self-excitation, higher efficiency and improved reliability [1].

The field-oriented control (FOC) concept is often used to produce a decoupled control of the torque and flux in the machine. To ensure a good operation at variable speed, FOC requires continuous and accurate information of the rotor position and speed. Therefore, either an encoder placed on the machine shaft or a programmed observer is necessary to acquire this information. In general, sensor-based encoders for position and speed have several drawbacks including hardware complexity, cost, sensitivity to external factors such as vibration and temperature [2, 3]. Hence, extensive research has focused on the design of software observers. These observers can be broadly classified into three categories according to the operating regime of the machine. The observers of the first family are operated only at nominal and medium speed, they are based on the machine standard model. The authors in [4] used the electromotive forces (EMF) to estimate the rotor position. In case of noise, an extended Kalman filter (EKF) intervenes [5], which increases the calculation time. The model reference adaptive system (MRAS) is another popular observer based on the machine parameters [6, 7]. Robust nonlinear observers based on sliding-mode have been extensively used in recent years [8]. This observer is simple and robust against perturbations and parametric variations. However, this observer requires a low-pass filter, which introduces a delay and reduces the phase margin of the system. Moreover, it needs an additional compensation of the position [9, 10]. The presence of chattering phenomenon can also deteriorate the performance of the mechanical systems because of excessive energy consumption and can lead to instability of the system [11]. To reduce the chattering phenomenon, it is necessary to shift the problem of discontinuity due to the switching element of the law in sliding regime on higher-order sliding variable derivatives. In [12] and [13], a super-twisting sliding mode observer (STSMO) was introduced to reduce the chattering. In

the presence of bounded perturbations, the super-twisting algorithm (STA) gives better results and faster convergence [14, 15]. In [16], it was shown that the STA cannot handle linearly growing perturbations and loses convergence. Hence, a modified STA is proposed in [9, 17] to compensate this disturbance type, however, the performance at low speed is not addressed in the paper.

The second category are the low-speed observers and most of these are based on the anisotropic effects. These observers can be classified according to the type of injected signal: (i) *High-frequency rotating signal injection* which can be classified into α−β frame rotating injection [18, 19, 20] or d−q frame rotating injection [21, 22]. It has been shown that the current injection requires the current regulators bandwidth to be greater than the injection frequency and the voltage signal injection was the most commonly used method. (ii) *Pulsating high-frequency signal injection* where, in the same way, the injected signal is a voltage [23] or a current [24] except that it is aligned with the d-axis or the estimated q-axis. Recently, in [25] the authors propose a new high-frequency (HF) pulsating signal injection into the stationary reference frame (α - β). In [26], the injected current pulses generate a noise which can reduce the accuracy of the estimation, the authors in [27] proposed using the two previous types, however, are independent of the machine parameters but produces more losses. In [28], it was shown that the precision of the position estimation is not satisfactory enough when using the indirect flux detection by On-line Reactance Measurement (INFORM) method. A square wave signal injection [29], and arbitrary injection [30] are other types of injected carrier signal. Injection methods add a current to the machine and therefore cause heating and vibrations during high-speed phases [31].

The observers of the last category are designed for wide speed range operation: Two approaches exist. The first consists of using two observers in a hybrid configuration with a transition algorithm. A hybrid structure, consisting of a flux observer with a signal-injection technique has been proposed in [20, 32]. However, at very low speed the dynamic

performance is not satisfactory and is not presented in sufficient details. In [21], the d−q frame persistent HF rotating carrier injection algorithm and a sliding mode observer (SMO) are combined by a weighting function, however, the direct torque control (DTC) produces high torque and flux ripples. In [31], the High frequency signal injection (HFSI) technique is associated with an adaptive SMO but this configuration requires a band-pass (BPF) and low-pass filter (LPF). A combination of a HF injection technique and a model–based technique are presented by [33] using a weighted average method. The authors in [22] proposed a hybrid position estimation combining the HFSI method with a classical SMO, however, the major drawback is the presence of LPF. In [3, 22, 23], a weighting coefficients switching method is used. It is worth noting that all these observer types have been proposed only for synchronous machines with non-uniform air gap. The observer, on the other hand, operates directly over a wide speed range and does not need a transition algorithm [34, 41].

In this paper, a new hybrid observer is proposed for the estimation of the rotor position and speed of a non-salient pole PMSG driven by a wind turbine and operating over a wide speed range. The HOSM observer is based on a modified super-twisting algorithm. The observer gains are designed to compensate linearly growing perturbations. This proposed observer structure is able to extract the mechanical effect (i.e. position and speed) at nominal and medium wind speed. However, these observers are mainly dependent on the amplitude of the EMF, which explains the degradation of the estimation performance at low speeds. The best known estimation methods at low speed among the existing ones are only suitable for salient pole machines. For this reason, another type of observer is proposed in [34] and adapted with the non-salient pole PMSG. The speed was determined from the quadrature flux and regulated using a classical PI controller and a fuzzy logic controller by imposing a direct reference current different from zero. The advantage of this observer structure is that it does not degrade the performance of the generator at high speeds. The introduction of weighting factors is necessary to select and combine these two observers in order to improve the signal of the

transition region according to the operating speed of the generator. The stability of each observer is established by Lyapunov method with an appropriate Lyapunov function. The performance of the proposed hybrid observer is evaluated via simulations with PI and fuzzy logic controllers at low speed and a comparison between the classical and the proposed observers is presented to demonstrate the effectiveness of the hybrid structure and switching strategy. This paper is organized in six sections. Section 2 describes the models of the wind turbine and PMSG. Section 3 presents the stator-side control scheme implemented in the model. The detailed derivation of the hybrid observer and switching algorithm are presented in Section 4 and 5 respectively. Section 6 presents the simulation results. Finally, the conclusions on this paper are summarized in Section 7.

2. Modeling of the Wind Power Generation System

The wind power system considered in this study consists of a wind turbine, a PMSG, a converter composed of a rectifier and an inverter separated by a dc bus and a three phase current filter connected to grid as depicted in Figure 1. The wind turbine drives the PMSG at a variable-speed through a gearbox [4, 5]. The focus of this study is on the selected part (dotted-line) of the Figure 1 which represents the wind conversion system.

2.1. Turbine Model

The mechanical power appearing at the rotor of the wind turbine driving a generator through a gearbox can be written as follows:

$$P_m = \frac{1}{2} C_p(\lambda) \rho \pi R^2 V_w^3 \tag{1}$$

Where ρ is the air density (kg/m^3), R is the blade radius (m), V_w is the wind speed (m/s) and C_p is the power coefficient. The value of C_p depends on the tip speed ratio (λ), the pitch angle (β) and the positive constants c_1 to c_6 [36].

$$C_p = c_1 \left(\frac{c_2}{\lambda_i} - c_3 \beta - c_4 \right) e^{\frac{-c_5}{\lambda_i}} + c_6 \lambda \tag{2}$$

With

$$\frac{1}{\lambda_i} = \frac{1}{\lambda + 0.08\beta} - \frac{0.035}{\beta^3 + 1} \tag{3}$$

And $C_p = 0.38, \beta = 0, \lambda_{opt} = 6.1, c_1 = 0.22, c_2 = 116, c_3 = 0.4, c_4 = 5, c_5 = 12.5, c_6 = 0$

The role of the gearbox coupling the wind turbine to the generator is to adapt the turbine speed ω_t with the generator speed ω_g. It is modeled as follows [47]:

$$\omega_t = \frac{1}{G}\omega_g \tag{4a}$$

$$\mathcal{T}_g = \frac{1}{G}\mathcal{T}_t \tag{4b}$$

Where $\mathcal{T}_t$ is the turbine torque, $\mathcal{T}_g$ is the generator torque and G is the gearing ratio.

2.2. The model of PMSG

The PMSG model in the stationary reference frame (α, β) attached to the stator, is written as:

$$\begin{cases} v_\alpha = -R_s i_\alpha - L_s \dfrac{di_\alpha}{dt} + e_\alpha \\ v_\beta = -R_s i_\beta - L_s \dfrac{di_\beta}{dt} + e_\beta \end{cases} \tag{5}$$

Where $v_{\alpha\beta}$ are stator terminal voltages, R_s and L_s denote the stator resistance and inductance respectively, $i_{\alpha\beta}$ represent the stator currents and $e_{\alpha,\beta}$ are the back EMFs which are given by:

$$\begin{cases} e_\alpha = -\omega_r \varphi_{pm} \sin\theta \\ e_\beta = \omega_r \varphi_{pm} \cos\theta \end{cases} \tag{6}$$

Where ω_r, θ and φ_{pm} are the rotor speed, rotor position and magnetic flux linkage respectively. The electromagnetic torque and the mechanical equation can be written as:

$$\mathcal{T}_{em} = n_p K_e \left(i_\beta \cos\theta - i_\alpha \sin\theta\right) \tag{7}$$

$$\frac{d\omega_r}{dt} = n_p K_e \left(i_\beta \cos\theta - i_\alpha \sin\theta\right) - \frac{f_v}{\mathcal{J}}\omega_r - \frac{\mathcal{T}_t}{\mathcal{J}} \tag{8}$$

Where $\mathcal{J}$ is the inertia, f_v is the viscous friction and $\mathcal{T}_t$ is the mechanical torque.

$K_e = \sqrt{\frac{3}{2}}\varphi_{pm}$ is the EMF constant and n_p is the pole pair number [37].

3. Stator-Side Converter Control

The basic structure of the control scheme is to decompose the stator current into two parts, one component controls the flux and the other component controls the torque. The speed regulation is used to control the torque at the same time to extract the maximum power from the turbine using a maximum power point tracking (MPPT) strategy. The speed reference depends on the wind speed and the optimal tip speed ratio is given by

$$\omega^* = \frac{\lambda_{opt} \times V_w}{R} \tag{9}$$

Were λ_{opt} is the optimal tip speed ratio and V_w is the wind speed (m/s).

Figure 2 shows the various control blocks on the generator side [7]. The estimated speed is regulated through the external loop while the internal loop controls the I_q current component. The I_d current component, on the other hand, is controlled at a reference current I_{dref} ($I_{dref} \neq 0$ at low speed and $I_{dref} = 0$ otherwise). In contrast, the current I_{qref} along the quadrature axis q is extracted from the speed regulator output, which is proportional to the electromagnetic torque. The outputs of current regulators are combined with the decoupling block to generate the reference voltages ($v_{\alpha ref}, v_{\beta ref}$). The space vector modulation (SVM) is applied to transform these references voltages into pulse width modulation (PWM) signals to control the inverter switches. The first observer (HOSM) estimates the rotor position and velocity from voltages and currents measurements in a fixed reference frame (α, β), while the second observer estimates the mechanical variables from voltages and currents in the rotating frame (d, q). The switching between the two observers is achieved by a transition bridge.

4. Design of the Observers

4.1. Super-Twisting Sliding Mode Observer

This observer is based on the classical variable structure theory. The aim is to generate a second order sliding regime on a correctly chosen surface to constrain the system trajectories to be evaluated after a finite time on the set $\{S = \dot{S} = 0\}$. It is characterized by the rotation of

the trajectories around the origin of the phase diagram [38, 39].

The standard model of STA can be represented by:

$$\dot{x}_1 = -\hbar_1 |\bar{x}_1|^{1/2} sign(\bar{x}_1) + x_2 + \delta_1(x_1, t) \quad (10a)$$

$$\dot{x}_2 = -\hbar_2 sign(\bar{x}_1) + \delta_2(x_2, t) \quad (10b)$$

Where x_i are the state variables, $\bar{x}_i$ are the errors between state variables, $\hbar_i$ represent the sliding coefficients, δ_i are perturbation terms and $sign(\cdot)$ is the sign function.

If the following conditions are satisfied, then STA-SMO converges in a finite time:

$$\hbar_1 > 2\mathfrak{h}_1, \quad \hbar_2 > k_1 \frac{5\mathfrak{h}_1\hbar_1 + 4\mathfrak{h}_1^2}{2(\hbar_1 - 2\mathfrak{h}_1)} \quad (11)$$

$$|\delta_1| \leq \mathfrak{h}_1\sqrt{|x_1|}, \quad \delta_2 = 0 \quad (12)$$

Where $\mathfrak{h}_1$ is a positive constant [16, 41].

4.2. Higher-Order Sliding Mode Observer for PMSG

This observer estimates the mechanical quantities (speed, position) from the EMFs estimation. The only inputs data provided to this observer are the stator currents and voltages measurements. To apply the STSM algorithm to the PMSG, the model of the machine given in (5) should be modified as follows:

$$\frac{d\hat{\imath}_\alpha}{dt} = \frac{-R_s}{L}\hat{\imath}_\alpha - \frac{1}{L}v_\alpha + \frac{1}{L}u_\alpha(t) \quad (13a)$$

$$\frac{d\hat{\imath}_\beta}{dt} = \frac{-R_s}{L}\hat{\imath}_\beta - \frac{1}{L}v_\beta + \frac{1}{L}u_\beta(t) \quad (13b)$$

Where $\hat{}$ denotes estimated value, and $L = L_d = L_q$.

Comparing with (5) and (6), it can be noticed that $\frac{-R_s}{L}\hat{\imath}_\alpha - \frac{1}{L}v_\alpha$ and $\frac{-R_s}{L}\hat{\imath}_\beta - \frac{1}{L}v_\beta$ in the PMSG voltage equations are considered as perturbation terms. $u_{\alpha,\beta}(t)$ are the robust terms based on the classical STA [41] defined as :

$$u_\alpha(t) = -\mathcal{K}_1 |\mathcal{S}_\alpha(t)|^{\frac{1}{2}} sign\big(\mathcal{S}_\alpha(t)\big) - \mathcal{K}_2 \int sign\big(\mathcal{S}_\alpha(t)\big)dt \quad (14)$$

Similarly, $u_\beta(t)$ can be obtained by replacing α with β.

The sign function limit can slow down the trajectories of the system when they tend to move away from the origin. Therefore, some linear terms are introduced to improve the convergence rate and make the sliding surface insensitive to the increasing perturbations. The following new correction terms are proposed [17, 9]:

$$\mathcal{u}_\alpha(t) = -\mathcal{K}_1\psi_1\big(\mathcal{S}_\alpha(t)\big) - \mathcal{K}_2\int \psi_2\big(\mathcal{S}_\alpha(t)\big)dt \tag{15}$$

In the same way, $\mathcal{u}_\beta(t)$ is obtained by replacing α with β.

The sliding surfaces are chosen as:

$$\mathcal{S}_\alpha(t) = \hat{\imath}_\alpha - i_\alpha \tag{16a}$$

$$\mathcal{S}_\beta(t) = \hat{\imath}_\beta - i_\beta \tag{16b}$$

Where $\hat{\imath}_\alpha$ and $\hat{\imath}_\beta$ are the estimated currents, i_α and i_β are the actual currents.

To compensate for linearly increasing perturbations, the nonlinear stabilizing terms $\psi_1\left(\mathcal{S}_{\alpha\beta}(t)\right)$, $\psi_2\left(\mathcal{S}_{\alpha\beta}(t)\right)$ are introduced and are defined by:

$$\psi_1\big(\mathcal{S}_\alpha(t)\big) = \mathcal{S}_\alpha(t) + K_3\sqrt{|\mathcal{S}_\alpha(t)|}\tanh\big(\mathcal{S}_\alpha(t)\big) \tag{17a}$$

$$\psi_2\big(\mathcal{S}_\alpha(t)\big) = \mathcal{S}_\alpha(t) + \tfrac{1}{2}\mathcal{K}_4^2\tanh\big(\mathcal{S}_\alpha(t)\big) + \tfrac{3}{2}\mathcal{K}_4\sqrt{|\mathcal{S}_\alpha(t)|}\tanh\big(\mathcal{S}_\alpha(t)\big) \tag{17b}$$

Similarly, the functions $\psi_1\left(\mathcal{S}_\beta(t)\right)$ and $\psi_2\left(\mathcal{S}_\beta(t)\right)$ can be obtained by replacing $\mathcal{S}_\alpha(t)$ with $\mathcal{S}_\beta(t)$ in (17a, 17b) [17].

Where $\mathcal{K}_1$,$\mathcal{K}_2$,$\mathcal{K}_3$ and $\mathcal{K}_4$ are design positive constants. The gain $\mathcal{K}_1$ can cause saturation when it is high. $\mathcal{K}_2$ and $\mathcal{K}_3$ are chosen to improve the stability in finite time and to reject the uncertainties effect. The gain $\mathcal{K}_4$ should be adjusted achieve a balance between robustness and chattering, $\mathcal{K}_1\psi_1\big(\mathcal{S}_\alpha(t)\big)$ is utilized to improve convergence time when trajectories are far from the origin, and $\mathcal{K}_2\psi_2\big(\mathcal{S}_\alpha(t)\big)$ will dominate the perturbation [9].

4.2.1 Sliding Mode Stability

To analyze the stability, the time derivatives of the sliding surface are determined from (5) and (13) as follow [40]:

$$\dot{\hat{\mathcal{S}}}_\alpha = \frac{-R_s}{L}\hat{\mathcal{S}}_\alpha - \frac{1}{L}e_\alpha + \frac{1}{L}u_\alpha(t) \quad (18a)$$

$$\dot{\hat{\mathcal{S}}}_\beta = \frac{-R_s}{L}\hat{\mathcal{S}}_\beta - \frac{1}{L}e_\beta + \frac{1}{L}u_\beta(t) \quad (18b)$$

Assumption 1: There exist two constants $\varrho_{\alpha,\beta}$ such that the disturbances terms are bounded as follows:

$$|\dot{e}_\alpha| \leq \varrho_\alpha \quad (19a)$$

$$|\dot{e}_\beta| \leq \varrho_\beta \quad (19b)$$

Since ω_s ,$\mathcal{T}_l$, $e_{\alpha,\beta}$ and $i_{\alpha,\beta}$ are continuous on a compact set, the condition (14) is not restrictive.

Theorem 1: According to Assumption 1, the origin of system in (18a, 18b) is robust and globally stable equilibrium point in a finite time. Further, the estimation of the unknown input/perturbation $e(\mathcal{S},t)$ is given by $\mathcal{K}_2\int_0^t \psi_2(\mathcal{S}_1(t))dt$ after a finite-time.

***Proposition 1*:** Consider the matrix $\mathcal{A}_0$:

$$\mathcal{A}_0 = \frac{1}{L}\begin{bmatrix} -(\mathcal{K}_1 + R_s) & L \\ -\mathcal{K}_2 & 0 \end{bmatrix} \quad (20)$$

Where $\mathcal{K}_1 > 0$ and $\mathcal{K}_2 > 0$, so that $\mathcal{A}_0$ is Hurwitz matrix.

From (17a, 17b) and (18a, 18b), the system can be represented as [9]:

$$\dot{\mathcal{S}}_1 = \mathcal{S}_2 - \left(\frac{\mathcal{K}_1 + R_s}{L}\right)\left(\mathcal{S}_1 + \mathcal{K}_4\lceil\mathcal{S}_1\rceil^{1/2} sign(\mathcal{S}_1)\right) \quad (21a)$$

$$\dot{\mathcal{S}}_2 = -\frac{\mathcal{K}_2}{L}\left(\mathcal{S}_1 + \frac{\mathcal{K}_4^2}{2}sign(\mathcal{S}_1) + 3\frac{\mathcal{K}_4}{2}\lceil\mathcal{S}_1\rceil^{1/2} sign(\mathcal{S}_1)\right) + \frac{\dot{e}_{\alpha,\beta}}{L} \quad (21b)$$

With

$$\mathcal{S}_1 = \mathcal{S}_{\alpha,\beta} \;, \mathcal{S}_2 = \left(\frac{1}{L}\right)\left[e_{\alpha,\beta} - \mathcal{K}_2\int \psi_2(\mathcal{S}_1(t))dt\right] \quad (22)$$

From (13a) and (21a):

$$\mathcal{K}_4 = \mathcal{K}_1\mathcal{K}_3/(\mathcal{K}_1 + R_s) \quad (23)$$

Proof 1 [16]: based on (17b), if $\mathcal{S}_{\alpha,\beta} = \dot{\mathcal{S}}_{\alpha,\beta} = 0$, then $|\phi_2(s)| \geq \mathcal{K}_4^2/2$, and one gets:

$|\dot{e}(\mathcal{S},t)| \leq |\psi_2(\mathcal{S})|$, so $\mathcal{K}_4 \geq \sqrt{2\varrho_{\alpha,\beta}}$,

and

$$\mathcal{K}_3 \geq \sqrt{2\varrho_{1,2}}(\mathcal{K}_1 + R_s)/\mathcal{K}_1 \tag{24}$$

To prove the stability and the convergence in finite time, the following Lyapunov function in quadratic form is used [14]:

$$V(\xi) = \xi^T \mathcal{F} \xi \tag{25}$$

Where $\mathcal{F}$ is a constant, symmetric and positive definite solution of V Such that $\mathcal{F} = \mathcal{F}^T = \begin{bmatrix} \Gamma + 4\varepsilon^2 & -2\varepsilon \\ -2\varepsilon & 1 \end{bmatrix}$, $\Gamma > 0$ and $\varepsilon > 0$ and with a new state vector:

$$\xi = \begin{bmatrix} \mathcal{S}_1 + \mathcal{K}_4 [\mathcal{S}_1]^{1/2} sign(\mathcal{S}_1) \\ \mathcal{S}_2 \end{bmatrix} = \begin{bmatrix} \xi_1 \\ \xi_2 \end{bmatrix} \tag{26}$$

The derivative of the Lyapunov function is:

$$\dot{V}(s) = \dot{\xi}^T \mathcal{F} \xi + \xi^T \mathcal{F} \dot{\xi} \tag{27}$$

And the standard inequality for quadratic forms is given by:

$$\Gamma_{min}\{\mathcal{F}\}\|\xi\|^2 \leq \xi^T \mathcal{F} \xi \leq \Gamma_{max}\{\mathcal{F}\}\|\xi\|^2 \tag{28}$$

From (26), the Euclidean norm of ξ is:

$$\|\xi\|^2 = \mathcal{S}_1^2 + 2\mathcal{K}_4|\mathcal{S}_1|^{3/2} + \mathcal{K}_4^2|\mathcal{S}_1| + \xi_2^2 \tag{29}$$

From (28), note that the inequality :

$$\|\xi\| \leq \frac{V^{1/2}(\mathcal{S})}{\Gamma_{min}^{1/2}\{\mathcal{F}\}} \tag{30}$$

Using (29), $\|\xi\|$ can be written as:

$$\|\xi\|^2 \geq \mathcal{K}_4^2|\mathcal{S}_1| \tag{31}$$

While $\mathcal{K}_4 > 0$, then:

$$-\frac{\mathcal{K}_4}{\|\xi\|} \geq -|\mathcal{S}_1|^{-1/2} \tag{32}$$

When expressed along the trajectories of the system, the derivative of the Lyapunov function becomes:

$$\dot{V} = \left(1 + \frac{\mathcal{K}_4}{2}|\mathcal{S}_1|^{-1/2}\right)\xi^T(\mathcal{A}_0^T\mathcal{F} + \mathcal{F}\mathcal{A}_0)\xi + 2\xi^T\mathcal{F}\begin{bmatrix}0\\ \dot{e}\end{bmatrix} \tag{33}$$

Where $\mathcal{F}$ and $\mathcal{H}$ are related by the algebraic Lyapunov equation:

$$-\mathcal{H} = \mathcal{A}_0^T\mathcal{F} + \mathcal{F}\mathcal{A}_0 = -\begin{bmatrix}\mathcal{H}_1 & \mathcal{H}_2\\ \mathcal{H}_2 & \mathcal{H}_3\end{bmatrix} \tag{34}$$

$\mathcal{H} = \mathcal{H}^T > 0$ is arbitrary, symmetric and positive definite matrix and l represent the feedback gain matrix. From proof 1, one can note that:

$$\dot{V} \leq \left(1 + \frac{\mathcal{K}_4}{2}|\mathcal{S}_1|^{-1/2}\right)\left(\xi^T(\mathcal{A}_0^T\mathcal{F} + \mathcal{F}\mathcal{A}_0)\xi + 2\xi^T\mathcal{F}\begin{bmatrix}0\\ \xi_1\end{bmatrix}\right)$$

$$\leq -\left(1 + \frac{\mathcal{K}_4}{2}|\mathcal{S}_1|^{-1/2}\right)\xi^T\mathcal{H}\xi \tag{35}$$

From (28), it implies that:

$$\dot{V} \leq -\left(1 + \frac{\mathcal{K}_4}{2}|\mathcal{S}_1|^{-1/2}\right)\Gamma_{min}(\mathcal{H})\|\xi\|^2 \tag{36}$$

With

$$\begin{cases}\mathcal{H}_1 = 2\left(\dfrac{\mathcal{K}_1 + R_s}{L}\right)(\Gamma + 4\varepsilon^2) - 4\varepsilon\left(\dfrac{\mathcal{K}_2}{L} - 1\right)\\ \mathcal{H}_2 = -2\varepsilon\left(\dfrac{\mathcal{K}_1}{L} + \dfrac{R_s}{L}\right) + \left(\dfrac{\mathcal{K}_2}{L} + 1\right) - (\Gamma + 4\varepsilon^2)\\ \mathcal{H}_3 = 4\varepsilon\end{cases} \tag{37}$$

For $\mathcal{H}$ to be positive, $\mathcal{K}_2$ and $\mathcal{K}_1$ should be such that:

$$\mathcal{K}_2 = L\left(\Gamma + 4\varepsilon^2 + \frac{2}{L}(\mathcal{K}_1 + R_s)\right) \tag{38}$$

$$\mathcal{K}_1 > -R_s + \frac{1}{\Gamma}(2\varepsilon L\Gamma - 2\varepsilon L + 8L\varepsilon^3) \tag{39}$$

Hence,

$$\dot{V} \leq -\mu_1 V^{1/2}(\mathcal{S}) - \mu_2 V(\mathcal{S}) \tag{40}$$

With $\mu_1 = \frac{\Gamma_{min}(\mathcal{H})}{\Gamma_{max}^{1/2}(\mathcal{F})}\frac{\mathcal{K}_4^2}{2}$ and $\mu_2 = \frac{\Gamma_{min}(\mathcal{H})}{\Gamma_{max}(\mathcal{F})}$

Where Γ_{max} and Γ_{min} represents respectively the maximum and minimum singular values of matrix $\mathcal{F}$ [14, 17, 42].

4.2.2 Convergence Time

The solution of the differential equation (40) is given by :

$$V(t)=\begin{cases}(V^{1/2}\left(\mathcal{S}_{\alpha,\beta}(t_0)\right)-\dfrac{\mu_1}{2}t)^2 & if\ \mu_1=1,\ \mu_2=0\\ e^{-\mu_2 t}(V^{1/2}\left(\mathcal{S}_{\alpha,\beta}(t_0)\right)+\dfrac{\mu_1}{\mu_2}\left(1-e^{\frac{\mu_2}{2}t}\right))^2 & if\ \mu_1\geq 0,\ \mu_2>0\end{cases} \quad (41)$$

At time $t=0$ the system trajectory (21a, 21b) starting at $\mathcal{S}_{\alpha,\beta}(t_0)$ will converge to the origin ($\mathcal{S}_{\alpha,\beta}=0$) in a finite time.When $\mu_1=1$ all trajectories converge to the origin in finite time, and when $\mu_1=0$ the convergence is exponential. From (41) the convergence time can be written as [14. 16] :

$$T=\begin{cases}\dfrac{2V^{1/2}\left(\mathcal{S}_{\alpha,\beta}(t_0)\right)}{\mu_1} & if\ \mu_2=0\\ \dfrac{2}{\mu_2}ln\left(\dfrac{\mu_2}{\mu_1}V^{1/2}\left(\mathcal{S}_{\alpha,\beta}(t_0)\right)+1\right) & if\ \mu_2>0\end{cases} \quad (42)$$

4.2.3 Speed and Rotor Position Estimation

When STA-SMO reaches the equilibrium point, this means that $\mathcal{S}_{\alpha,\beta}=\dot{\mathcal{S}}_{\alpha,\beta}=0$ in finite time, equation (18a, 18b) becomes:

$$0=-\mathcal{K}_2\int_0^t\psi_2(\mathcal{S}_\alpha(t))dt+\hat{e}_\alpha \quad (43a)$$

$$0=-\mathcal{K}_2\int_0^t\psi_2\left(\mathcal{S}_\beta(t)\right)dt+\hat{e}_\beta \quad (43b)$$

Then, the estimated back-EMF can be obtained as follows:

$$\hat{e}_\alpha=K_2\int_0^t\psi_2(\mathcal{S}_\alpha(t))dt \quad (44a)$$

$$\hat{e}_\beta=K_2\int_0^t\psi_2\left(\mathcal{S}_\beta(t)\right)dt \quad (44b)$$

Equation (6) shows that there is a relation between the EMF and the rotor position, so it is expressed by:

$$\hat{\theta}_1 = -tan^{-1}\left(\frac{\hat{e}_\alpha}{\hat{e}_\beta}\right) \tag{45}$$

The expression of the estimated speed is deduced from the EMFs as follows [9]:

$$\hat{\omega}_1 = \frac{1}{k_e}\sqrt{\hat{e}_\alpha^2 + \hat{e}_\beta^2} \tag{46}$$

4.3. Design of the Second Observer

The HOSMO described in the previous section is suitable for medium and high speed sensorless operation, where the electromotive force (EMF) can be easily estimated. However, at low speed, this EMF is very small which leads to a poor estimation performance and the effects of inverter nonlinearity become severe [16, 41]. To alleviate this problem, another approach is proposed.

The approach adopted in this observer is based on the injection of a non-zero direct current. The principle is to force this current in the defective position, and this will force the position of the rotor to the incorrectly estimated position, and consequently the error between the actual and the estimated position will be reduced [34]. The velocity is obtained from the imaginary part of the flux using two control methods: a classical PI controller and a fuzzy logic controller as shown in Figure 3. The position is the integral of this velocity. The current and voltage are expressed with a complex space phasors as follow:

$$i_s = \frac{2}{3}(i_a + ai_b + a^2 i_c) \tag{47}$$

$$v_s = \frac{2}{3}(v_a + av_b + a^2 v_c) \tag{48}$$

a and a^2 are the spatial operators, where $a = e^{j2\pi/3}$. The flux equations are given by [43]:

$$\begin{cases} \dot{\varphi}_s = v_s - R_s i_s \\ \varphi_s = L i_s + \varphi_r \\ \varphi_r = \varphi_m e^{j\theta} \end{cases} \tag{49}$$

The voltage of the PMSG expressed in the coordinate related to the rotor is given by [34]:

$$v_s^{(R)} = -Ri_s^{(R)} - (S + \jmath\omega_2)Li_s^{(R)} + \jmath\omega\varphi_m \tag{50}$$

Where S is the time derivative operator. The voltage equation in the coordinate system $e^{\jmath\hat{\theta}_2}$ becomes:

$$v_s^{(\hat{R})} = -R_s i_s^{(\hat{R})} - (S + \jmath\hat{\omega}_2)\left(Li_s^{(\hat{R})} - \varphi_m e^{\jmath(\theta-\hat{\theta}_2)}\right) \tag{51}$$

Where $\hat{\omega}_2 = S\hat{\theta}$. Let $\tilde{\theta} = \hat{\theta}_2 - \theta$, thus:

$$e^{j\tilde{\theta}} = \cos\tilde{\theta} + \jmath\sin\tilde{\theta} \tag{52}$$

Substituting (52) into (51) gives after simplifications:

$$\varphi_m - Li_s = \frac{1}{S + \jmath\hat{\omega}_2}\left(v_s + R_s i_s + \left(\omega\sin\tilde{\theta} + \jmath\left(\omega\cos\tilde{\theta} - \hat{\omega}_2\right)\right)\varphi_m\right) \tag{53}$$

The observer may take the following form:

$$\hat{\varphi}_r - Li_s = \frac{1}{S + \jmath\hat{\omega}_2}(v_s + R_s i_s + Q) \tag{54}$$

By subtracting (53) from (54), the flux dynamic error is obtained as:

$$S(\hat{\varphi}_r - \varphi_m) = -\jmath\hat{\omega}_2(\hat{\varphi}_r - \varphi_m) + Q + \left(\omega\sin\tilde{\theta} + \jmath\left(\omega\cos\tilde{\theta} - \hat{\omega}_2\right)\right)\varphi_m \tag{55}$$

Where $\hat{\varphi}_r = \hat{\varphi}_{rd} + \jmath\hat{\varphi}_{rq}$

Stabilizing with $Q = -\mathcal{C}_1(\hat{\varphi}_{rd} - \varphi_m) - \mathcal{C}_2\hat{\varphi}_{rq}$, equation (55) is decomposed into a real and an imaginary part:

$$S(\hat{\varphi}_{rd} - \varphi_m) = -\mathcal{C}_1(\hat{\varphi}_{rd} - \varphi_m) + \hat{\omega}_2\hat{\varphi}_{rq} + \omega\sin\tilde{\theta}\,\varphi_m \tag{56}$$

$$S\hat{\varphi}_{rq} = -\mathcal{C}_2\hat{\varphi}_{rq} - \hat{\omega}_2(\hat{\varphi}_{rd} - \varphi_m) - \left(\hat{\omega}_2 - \omega\cos\tilde{\theta}\right)\varphi_m \tag{57}$$

With $\hat{\varphi}_{rq} = \varphi_m\sin\tilde{\theta}$, and $\hat{\varphi}_{rd} = \varphi_m\cos\tilde{\theta}$, (56, 57) become :

$$S(\hat{\varphi}_{rd} - \varphi_m) = -\mathcal{C}_1(\hat{\varphi}_{rd} - \varphi_m) + \hat{\omega}_2\hat{\varphi}_{rq} - \omega\hat{\varphi}_{rq} \tag{58}$$

$$S\hat{\varphi}_{rq} = -\mathcal{C}_2\hat{\varphi}_{rq} - \hat{\omega}_2(\hat{\varphi}_{rd} - \varphi_m) - (\hat{\omega}_2 - \omega)\varphi_m + \omega(\hat{\varphi}_{rd} - \varphi_m) \tag{59}$$

Replacing $\tilde{\omega} = \hat{\omega}_2 - \omega$ in (58, 59) gives:

$$S(\hat{\varphi}_{rd} - \varphi_m) = -\mathcal{C}_1(\hat{\varphi}_{rd} - \varphi_m) + \tilde{\omega}\hat{\varphi}_{rq} \tag{60}$$

$$S\hat{\varphi}_{rq} = -\mathcal{C}_2\hat{\varphi}_{rq} - \tilde{\omega}(\hat{\varphi}_{rd} - \varphi_m) - \tilde{\omega}\varphi_m \quad (61)$$

4.3.1. Stability Analysis

The stability is assessed using the following Lyapunov function:

$$\mathcal{P} = \frac{1}{2}\left((\hat{\varphi}_{rd} - \varphi_m)^2 + \left(\hat{\varphi}_{rq}\right)^2 + \frac{1}{\sigma}\tilde{\omega}^2\right) \quad (62)$$

The time derivative of the Lyapunov function $\mathcal{P}$ is obtained with arrangement of equations (60, 61) and (62) as:

$$\frac{d\mathcal{P}}{dt} = -\mathcal{C}_1(\hat{\varphi}_{rd} - \varphi_m)^2 - \mathcal{C}_2\left(\hat{\varphi}_{rq}\right)^2 + \tilde{\omega}\left(-\varphi_m\hat{\varphi}_{rq} + \frac{1}{\sigma}\frac{d\tilde{\omega}}{dt}\right) \quad (63)$$

If $\frac{d\tilde{\omega}}{dt} = \sigma\varphi_m\hat{\varphi}_{rq}$, equation (63) becomes:

$$\frac{d\mathcal{P}}{dt} = -\mathcal{C}_1(\hat{\varphi}_{rd} - \varphi_m)^2 - \mathcal{C}_2\left(\hat{\varphi}_{rq}\right)^2 \quad (64)$$

For $\mathcal{C}_1 > 0$ and $\mathcal{C}_2 > 0$, then:

$$\hat{\varphi}_r = \hat{\varphi}_{rd} + j\hat{\varphi}_{rq} \rightarrow \varphi_m \quad (65)$$

Under this condition, $\hat{\varphi}_{rq} = -\varphi_m \sin\tilde{\theta}$. Where $\hat{\theta}_2$ is approximated with θ ($\hat{\theta}_2 \equiv \theta$), using (63) to test the adaptation condition.

$$\frac{d\tilde{\omega}}{dt} = \sigma\varphi_m\hat{\varphi}_{rq} \quad (66)$$

Finally, if ω is supposed constant, equation (66) becomes:

$$\frac{d\hat{\omega}_2}{dt} = \sigma\varphi_m\hat{\varphi}_{rq} \quad (67)$$

4.3.2. Design of the PI Regulator

In practice if the speed variation is slow compared to the adaptation time constant, which depends on σ_2, then the speed ω can be considered as constant. Thus the observer becomes [34]:

$$\begin{cases} \hat{\varphi}_r = \hat{\varphi}_s - Li_s \\ \hat{\varphi}_s = \int_0^t \left(v_s + R_s i_s - \mathcal{C}_1(\hat{\varphi}_{rd} - \varphi_m) - j\mathcal{C}_2\hat{\varphi}_{rq} - j\hat{\omega}_2\hat{\varphi}_s\right)dt \\ \hat{\omega}_2 = \sigma_1\hat{\varphi}_{rq} + \sigma_2\int_0^t \hat{\varphi}_{rq}dt \\ \hat{\theta}_2 = \int_0^t \hat{\omega}_2\, dt \end{cases} \quad (68)$$

Where σ_1 and σ_2 are gains of the PI regulator, $\mathcal{C}_1$ and $\mathcal{C}_2$ are positive constants.

4.3.3. Design of the Fuzzy Controller

Classical PI controllers are very sensitive to internal parameters variations and external disturbances. Fuzzy logic controller (FLC), on the other hand, have attractive features such as robustness and hence overcomes these problems.

The FLC includes four basic components: fuzzification, fuzzy rule base, fuzzy inference engine and defuzzification [46].

For this system, the quadrature flux $\hat{\varphi}_{rq}$ and its change $d\hat{\varphi}_{rq}$ are the inputs of this FLC. The output represent the estimated speed, where the flux variation $d\hat{\varphi}_{rq}$ is defined by :

$$d\hat{\varphi}_{rq} = (\hat{\varphi}_{rq}(t+1) - \hat{\varphi}_{rq}(t))/T \quad (69)$$

Where T is the sampling period

Three membership functions with triangular and trapezoidal symmetrical equidistant shaps are defined for each input variable with the universe of discourses [-2, 2] for $\hat{\varphi}_{rq}$ and [-1.2, 1.2] for $d\hat{\varphi}_{rq}$ respectively. The output has nine triangular membership functions defined in the universe of discourse [-20, 20]. The membership functions for the inputs and outputs are shown in Figure 4. The fuzzy subset of linguistic variables are labelled as Negative Big (NB), Negative Small (NS), Negative (N), Negative Medium (NM), Zero (Z), Positive Medium (PM), Positive (P), Positive Small (PS), Positive Big (PB). All the fuzzy inference rules are summarized in Table 1, where the AND fuzzy operation intersection is applied between the inputs. The max Mamdani method was used in the inference mechanism. The center of

gravity was employed in the defuzzification, to transform the fuzzy set resulting from the rules aggregation into a control quantity, which represents the estimated speed:

$$\widehat{\omega}_2(k) = \frac{\sum_{i=1}^{n} U_i \, \mu[U_i]}{\sum_{i=1}^{n} [U_i]} \tag{70}$$

Where $\mu[U_i]$, n and U_i is the degree of membership value, the number of the fuzzy rules (equal to 9 in this case) and the center of gravity of the i^{th} fuzzy set respectively [44, 45]. k_1, k_2 and k_3 are adaptation gains which determine the transient and steady-state characteristics of the FLC controller [48].

The direct reference current at low speeds is changed and takes a non-zero value, which can be determined from [34] as:

$$i_{ref}^{d} = i_0^{d} e^{-\widehat{\omega}/\omega_0} \tag{71}$$

Where i_0^d is the maximum current and ω_0 is the low speed. These parameters i_0^d and ω_0 are determined from [34].

5. Switching Algorithm

The transition between the observers is achieved using two weighting coefficients α and η, as shown in Figure 5. Where α represents the weighting of the speed obtained at low regime, while η is the weighting of the speed obtained from HOSMO. α Fully prevails below a threshold speed $\Omega_1 = 9\,rad/s$, however, η dominates above a threshold speed $\Omega_2 = 25rad/s$. The transition is activated for a speed $\Omega_1 < \omega < \Omega_2$ where a common information are in this region.

It is important to note that the effectiveness of this method depends essentially on the choice of the transition region. This transition zone can be determined from the maximum speed above which the low speed observer performance deteriorates, and the minimum speed below which the HOSMO performance deteriorates [21, 23]. The classical algorithm [3, 23] imposes a single speed in each region. However, in case of divergence of one of the observer, the system remains in a poor performance until the intervention of the second observer, then

control is completely lost if no reference change is applied. The modified switching strategy overcomes these drawbacks and improves the performance of the system. The modified algorithm is illustrated in Figure 6.

6. Simulation Results

The simulation is performed in MATLAB/Simulink. To demonstrate the effectiveness of the proposed approach, the following wind profile is used:

$$V_w = 10 + 0.2\sin 0.1047t + 2\sin 0.2665t + \sin 1.2930t + 0.2\sin 3.664t \quad (72)$$

The low wind speed operation starts from $t = 0\ to\ 3.5s$ with a value of $0.1V_w$, the transition is applied during the acceleration. From $t = 4\ to\ 10s$ the wind nominal speed takes the value of V_w, then decreases back to the first value between $t = 11s$ and $t = 15.5s$. Finally, the wind speed changes its value from $0.1\ to\ 0.5V_w$ for the rest of the time. The perturbation changes under different operation conditions and its derivative is limited even if the perturbation is unbounded or varies over time. A large disturbance with low HOSMO coefficients can be lead to instability of system, small disturbance with HOSMO coefficients can cause chattering. For this reason, The rate limit of the perturbation change is given by $\varrho_{\alpha.\beta} = 4$, and the HOSMO coefficients are chosen to achieve a compromise between the robustness, convergence rate and the size of control action. Based on the basis of the following parameters :

$\varepsilon = 1, \varrho_{1,2} = 4, \Gamma = 0.02$. Where the HOSMO coefficients are calculated from (23), (24), (38) and (39) as :

$\mathcal{K}_1 = 0.5,\ \mathcal{K}_2 = 2.5, \mathcal{K}_3 = 8$ and $\mathcal{K}_4 = 3$.

(switching frequency is 15 kHz). The gains of the speed PI controller are set to: $kp_w = 0.2$ and $ki_w = 0.4$. $kp_i = 4$ And $ki_i = 570$. For the observer at low speed: $\sigma_1 = 100$ and

$\sigma_2 = 10$, $\mathcal{C}_1 = 250$ and $\mathcal{C}_2 = 5$. Table 2 give the various parameters values of the machine and turbine used in the simulation model.

The control associated with these observers guarantee a good transient and steady-state performance in the nominal, medium and low regime simultaneously at the transition region. From the first comparison, the FLC demonstrated better performance than PI control as shown in Figure 7 (right panel) and Figure 7 (left panel) respectively. Figure 7a shows that the estimated generator speed follows reasonably well its reference with good response characteristics and accuracy. There is no discontinuity between two speed regions, and there is almost no influence and no performance degradation confirming the effectiveness of the proposed observer structure and control scheme. Moreover, no chattering appeared at high speeds. Figure 7b indicates two separate speed regions where the low speeds are reserved only for the second observer and after 25 rad/s the HOSMO is activated. It can also be observed that the second observer during the high-speed region is about zero. Figure 7d shows the estimated rotor position, which can be clearly seen to track exactly the measured position. During this speed change, the electromechanical torque undergoes a sudden peak which then quickly vanishes as shown in Figure 8f. Note that these peaks are not expected to cause any damage to the machine. The results show that the FLC performance is superior to that of PI control and the peaks are even reduced. The current i_q has the same form as the torque, and the decoupling achieved was successfully by maintaining $i_d = 0$. The current i_d takes two different values $0A$ at high speed and $5A$ at low speed as depicted in Figure 7e. The optimal values of C_p and λ shown in Figure 8g clearly illustrate the performance of the MPPT, where Figure 7c shows the current components along α and β axes which have a sinusoidal shape. The three-phase currents i_{abc} is shown in Figure 7h. Finally, it can be seen that the signal with FLC improve the signal quality at transition region.

Figure 8A shows that the HOSMO loses its control in its region but, with the proposed algorithm, the observer at low speed continue to operate until HOSMO is activated again (Figure 8A left side). However, with the classical algorithm, HOSMO is selected despite the poor performance.

The transient speed response is better with the proposed new approach (Figure 8B, left side) than the original approach (Figure 8B, right side). In the (Figure 8C, left side), the proposed structure favors HOSMO even though it is not supposed to operate here. However, the classical structure maintains the second observer despite the deterioration of the response. After the comparison it can be observed that the two algorithms perform the same operation, but with the original algorithm, each observer is responsible to its region, this can cause unacceptable excursions that can cause damage the machine. On the contrary, the proposed algorithm is able to balance between the two observers and does not let the loss of control affect the performance of the machine. The performance of the proposed algorithm is acceptable in all phases.

Finally, Table 3 shows the comparison among five methods.As a summary, the advantages of the proposed method are the following: 1) Guaranteed at wide speed range; 2) Only for Non salient pol NSPPMSM; 3) Confirmed at wide speed range; 4) take into consideration the losing control; and 5) the position error in the transition zone is 0.06 (rad).

7. Conclusion

In this paper, a new hybrid observer is proposed to estimate the position and velocity of a non-salient pole permanent magnet synchronous generator (NSPPMSG) coupled to a wind turbine that operates over a wide speed range. The proposed hybrid observer consists of two observers coupled in cascade using a modified weighting coefficients method. The low-speed observer is specially adapted to this type of machine and is able to determine the mechanical effect caused by the quadrature axis rotor flux. The second observer, high order sliding mode observer operates at medium and nominal wind speed, which is designed based on a modified

structure of the super twisting algorithm. The second observer gains are designed such us to limit the impact of a linearly growing perturbation. The stability of each observer is guaranteed by Lyapunov stability analysis. The simulations results at low speed show that the fuzzy logic based regulator gives better performance than the classical PI regulator. Moreover, another comparison confirms the effectiveness of the proposed switching algorithm, and these results are satisfactory in the nominal, medium and low case scenarios and are the same at the transition region, where its show no influence under wind speed variations.

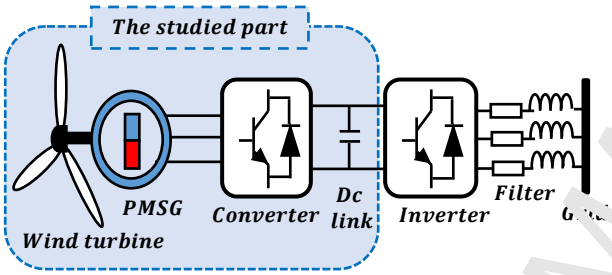

Fig.1. *Configuration of a PMSG wind turbine*

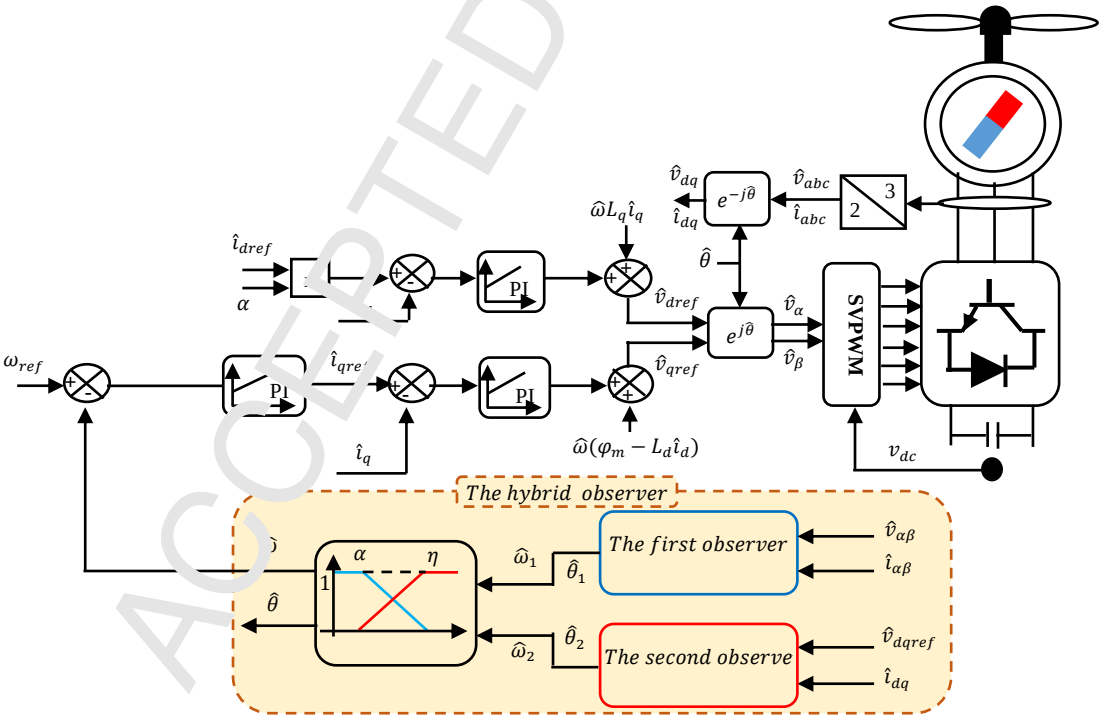

Fig.2. *Block diagram of the hybrid sensorless speed control.*

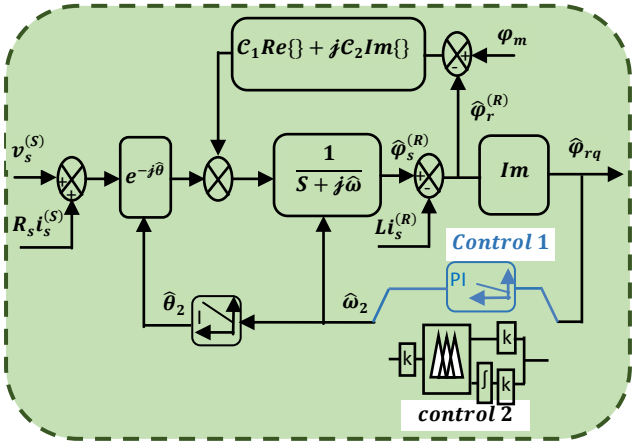

Fig. 3. *Second observer*

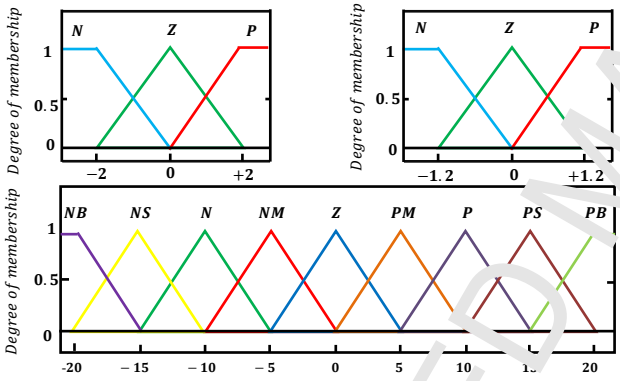

Fig. 4. *Membership functions of e ar u re pectively*

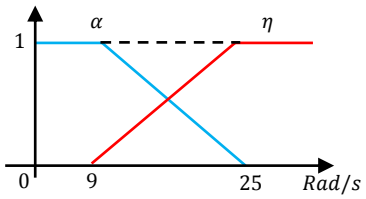

Fig. 5. *Weighting coefficients for switching algorithm*

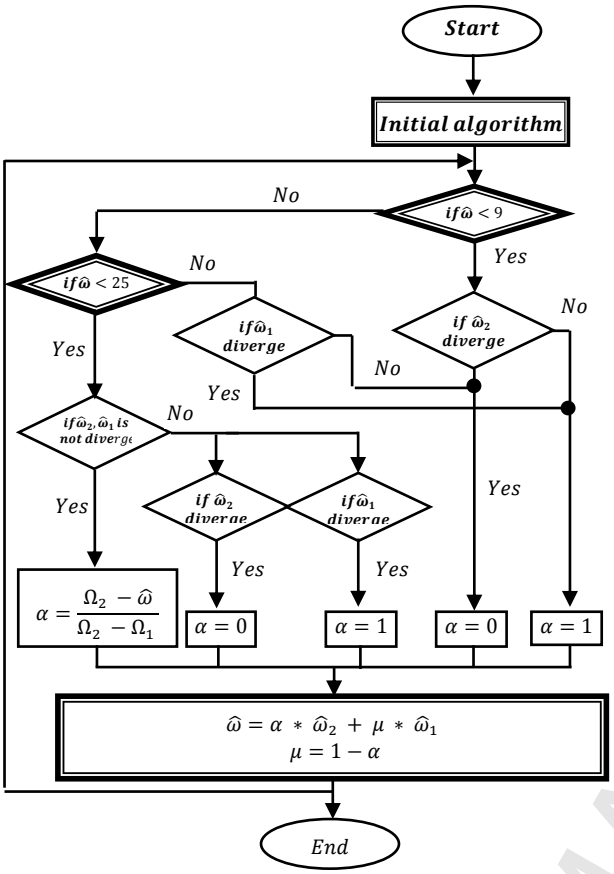

Fig. 6. *Proposed Switching Algorithm*

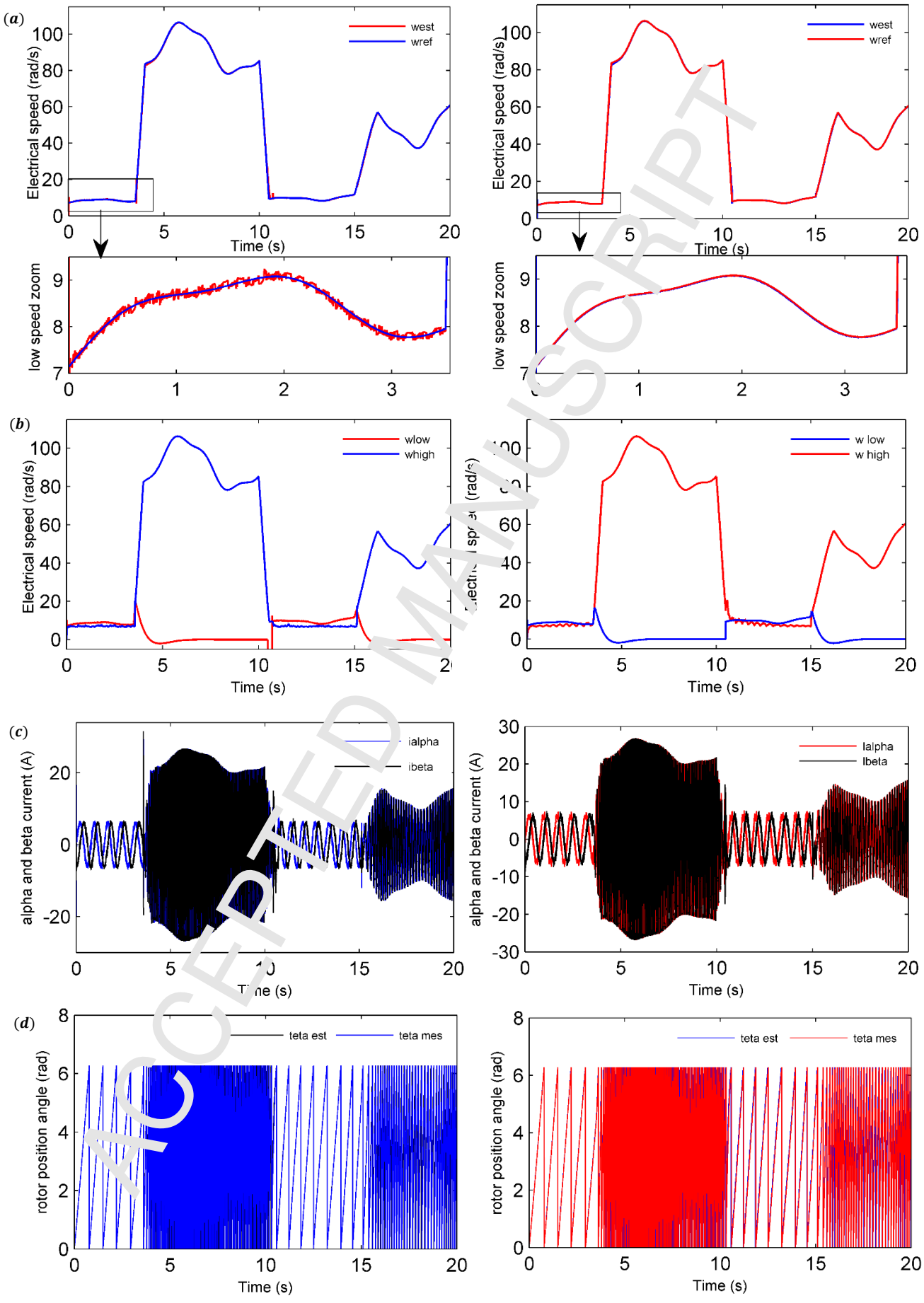

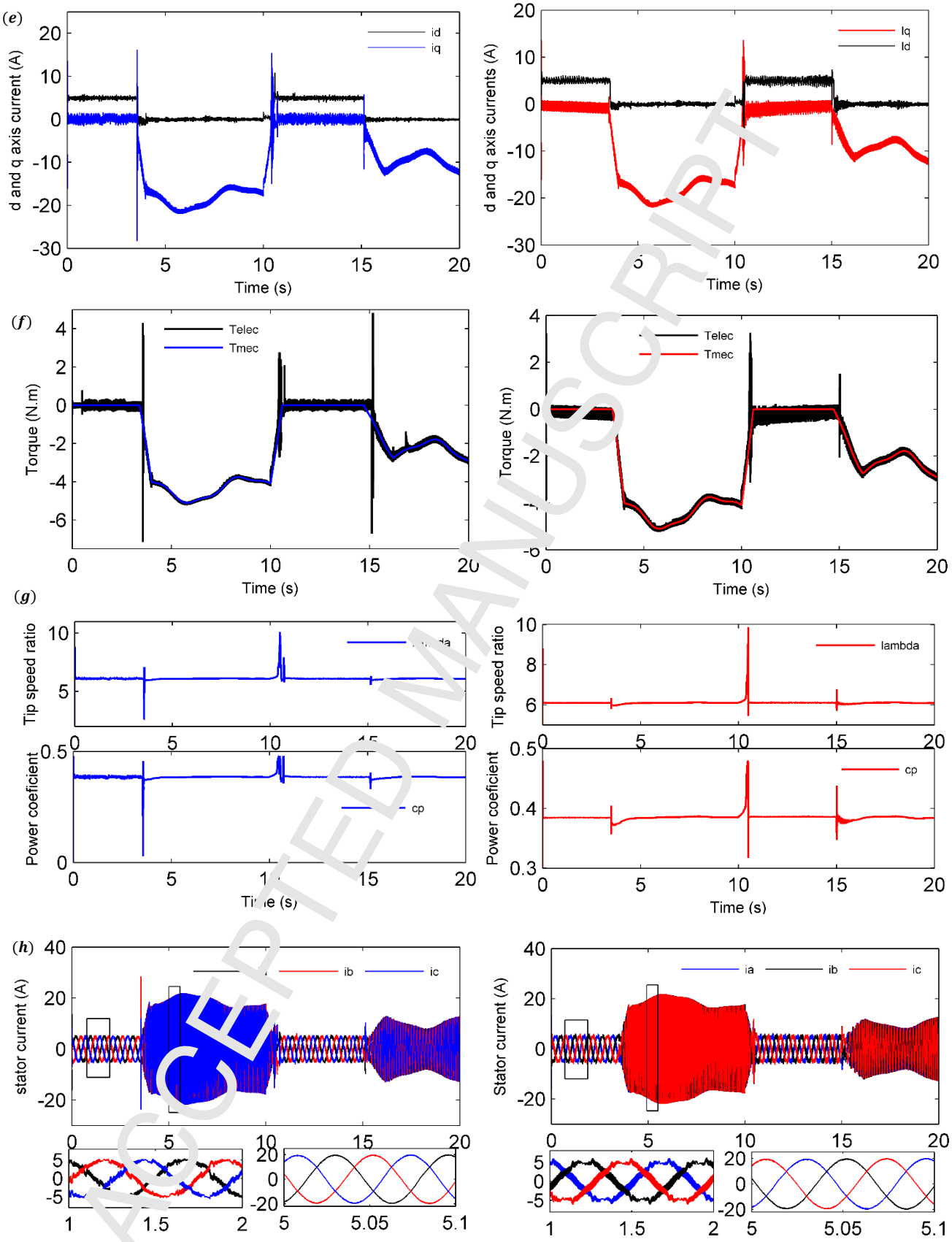

Fig.7. *(left side) PI controller; (right side) Fuzzy controller.*

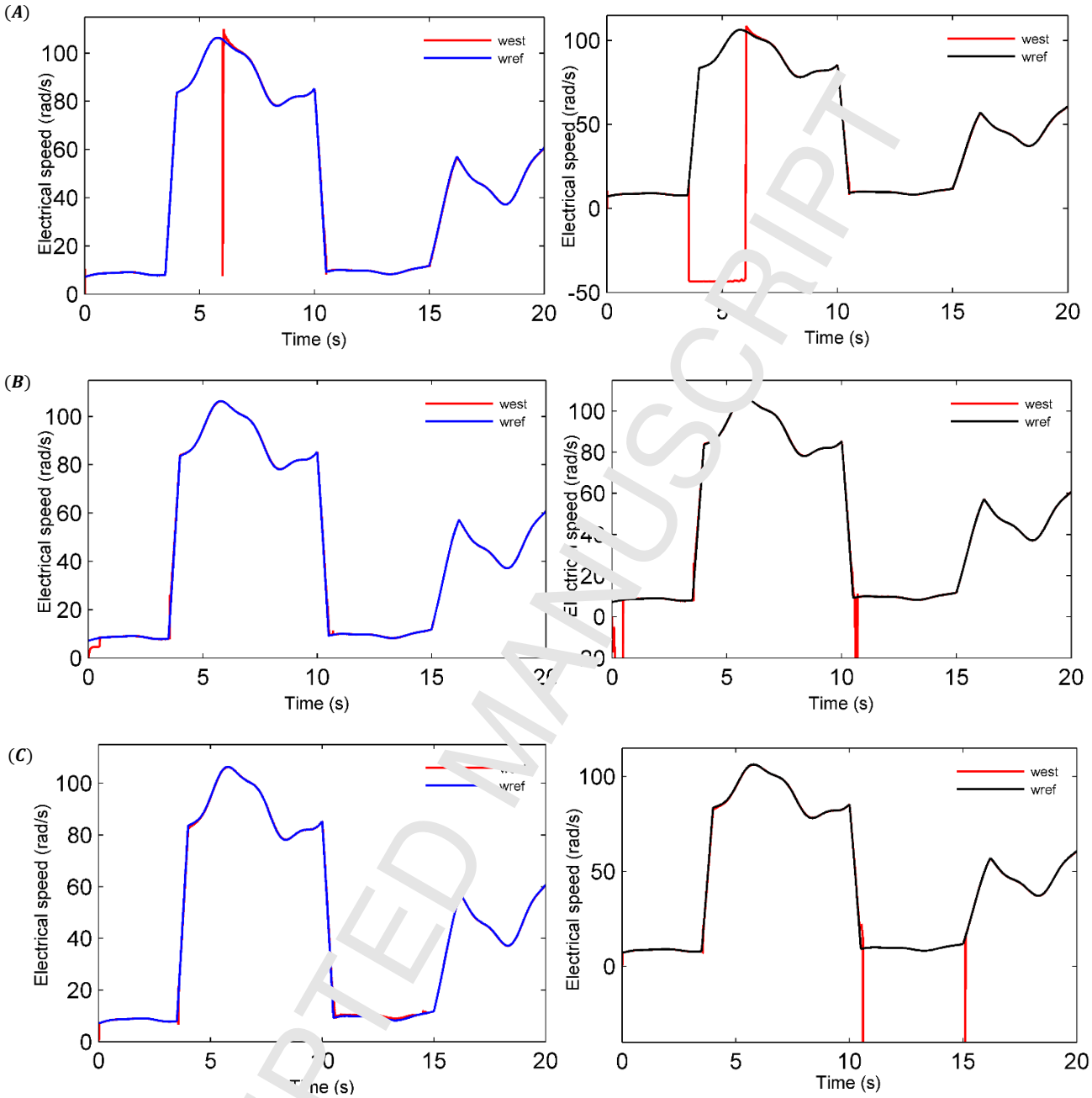

Fig. 8. (right side) traditional algorithm (left side) proposed algorithm.

Table 1 - Fuzzy control rule

du		$d\hat{\varphi}_{rq}$		
		N	**Z**	**P**
$\hat{\varphi}_{rq}$	**N**	NB	NS	P
	Z	NM	Z	PM
	P	N	PS	PB

Table 2 – A machine parameters.

Parameters	Values	Units
Stator Resistance Rs	0.57	[Ω]
Stator Inductance L	0.004	[H]
Back EMF constant K_e	0.078	$[Vs/rad]$
viscous friction f_v	0.004	$[Nm \cdot s/rad]$
Rotor flux ϕ_m	0.064	[wb]
Moment of Inertie J	0.002	$[Kg.m^{-2}]$
Number of pole paires np	2	

Table 3: Comparison between different approaches.

Performance criteria	comparison				
	Proposed approach	**[3]**	**[20]**	**[22]**	**[23]**
robustness	Guaranteed at wide speed range	robust at high speed	robust against parameter variation at high speed	robust against parameter variation at high speed	robust against parameter variation at high speed
simplicity	simple structure	simple structure	simple structure	complicated structure	simple structure
limitations	Only for Non salient pol NSPPMSM	For machine with $L_d \neq L_q$	For Surface Mounted PMSM	Only For interior PMSM	For Surface Mounted PMSM
stability	Confirmed at wide speed range	Not confirmed at low speed	Not confirmed	Not confirmed	Not confirmed at low speed
Losing control	take into consideration	No take into consideration	No take into consideration	No take into consideration	No take into consideration
Position error in the transition zone (rad)	0.06	0.12	0.08	0.07	0.1

REFERENCES

[1] Shengquan Li, Kezhao Zhang, Juan Li, Chao Liu, On the rejection of internal and external disturbances in a wind energyConversion system with direct-driven PMSG, ISA Trans. 61, (2016), 95-103.

[2] R. Fantino, J. Solsona, C. Busada, Non-lineair observer-based control for PMSG wind turbine, Energy 113 (2016) 248-257.

[3] I. Omrane, E. Etien, W. Dib, O. Bachelier, Modeling and simulation of soft sensor design for real-time speed and position estimation of PMSM, ISA Trans. 57 (2015) 329-339.

[4] S. Bolognani, S. Calligaro, R. Petrella, Design Issues and Estimation Errors Analysis of Back-EMF-Based Position and Speed Observer for SPM Synchronous Motors, IEEE

Journal of Emerging and Selected Topics in Power Electronics, 2 (June (2) (2014)) 159-170.

[5] D. Xu, S. Zhang, J. Liu, Very-low speed control of PMSM based on EKF estimation with closed loop optimized parameters, ISA Trans. 52 (2013) 835–843.

[6] Y. Shi, K. Sun, L. Huang, Y. Li, Online identification of permanent magnet flux based on extended kalman filter for ipmsm drive with position sensorless control, IEEE Trans. Ind. Electron. 59 (November (11)) (2012), 4169–4178.

[7] Z. Q. Guo, S. K. Panda, A Novel Design of Rotor Position Estimator for Sensorless Control of SPMSM Operating at Medium and High Speeds, IEEE PEDS 2015, Sydney, Australia, june 2015,pp 1080-1085.

[8] M. Pacas, Sensorless drives in industrial applications, IEEE Ind. Electron. Mag. 5 (june (2)) (2011), 16–23.

[9] S. K. Kommuri, M. Defoort, H. R. Karimi, K. C. Veluvolu, A Robust Observer-Based Sensor Fault-Tolerant Control for PMSM in Electric Vehicles, IEEE Trans. Ind. Electron.63 (December (12)) (2016), 7671 – 7681.

[10] Si Yi Chen, Ying Luo, YouGuo Pi, PMSM sensorless control with separate control strategies and smooth switch from low speed to high speed, ISA trans, 58, (2015), 650-658.

[11] H. Kim, J. Son, J. Lee, A high-speed sliding-mode observer for the sensorless speed control of a PMSM, IEEE Trans. Ind. Electron. 58 (September (9)) (2011), 4069–4077.

[12] Vasilios C. Iliouda, Chattering reduction applied in pmsm sensorless control using second order sliding mode observer, in Proc. 9th Int. Conf. Compat. Power Electron, June 2015, pp.240–245

[13] M. Ezzat, J. de Leon, N. Gonzalez, A. Glumineau, Observer controller scheme using high order sliding mode techniques for sensorless speed control of permanent magnet synchronous motor, in Proc. 49th IEEE Conf. Decision Control, Dec 2010, pp. 4012–4017.

[14] J.A. Moreno, "A linear framework for the robust stability analysis of a generalized super twisting algorithm, " 6th International Conference on Electrical Engineering, Computing Science and Automatic Control, Toluca, Mexico, 2009, pp. 12- 17.

[15] L. Zhao, J. Huang, H. Liu, B. Li, W. Kong, Second-order sliding mode observer with online parameter identification for sensorless induction motor drives, IEEE Trans. Ind. Electron, 61(October (10)) (2014), 5280–5289.

[16] J. A. Moreno, M. Osorio, Strict Lyapunov functions for the super-twisting algorithm, IEEE Trans. Automat. Control, 57 (April (4)) (2012), 1035–1040.

[17] T. Gonzalez, J. Moreno, L. Fridman, Variable gain super-twisting sliding mode control, IEEE Trans. Automat. Control, 57 (August (8)) (2012), 2100–2105.

[18] J. Lara, A. Chandra, Performance Investigation of Two Novel HSFSI Demodulation Algorithms for Encoderless FOC of PMSMs Intended for EV Propulsion, IEEE Trans. Ind. electron, 65 (July (2)) (2017), 1074 – 1083.

[19]Z. Q. Zhu, A.H. Almarhoon, P. L. Xu, Improved Rotor Position Estimation Accuracy by Rotating Carrier Signal Injection Utilizing Zero-Sequence Carrier Voltage for Dual Three-Phase PMSM, IEEE Trans. Ind. electron, 64 (May (6)) (2016), 4454 – 4462.

[20] C. Silva, G.M. Asher, and M. Sumner, Hybrid rotor position observer for wide speed range sensorless PM motor drives including zero speed, IEEE Trans. Ind. Electron. 53 (April (2)) (2006), 373 – 378.

[21] S. Sayeef, G. Foo, M. F. Rahman, Rotor position and speed estimation of a variable structure direct-torque-controlled IPM synchronous motor drive at very low speeds including standstill, IEEE Trans. Ind. Electron., 57 (November (11)) (2010), 3715–3723.

[22] G. Wang, R. Yang, D. Xu, DSP-Based Control of Sensorless IPMSM Drives for Wide-Speed-Range Operation, IEEE trans. Ind. electron, vol. 60 (February (2)) (2013), 720-727.

[23] Z Ma, J Gao, R. Kennel, FPGA Implementation of a Hybrid Sensorless Control of SMPMSM in the Whole Speed Range, IEEE trans. Ind. Inf., 9 (august (3)) (2013) 1253-

1261.

[24] W. Jianmin, Performance of pulsating high-frequency current injection based sensorless control of PMSM, In 2 nd International Symposium on Computer Communication Control and Automation (ISCCCA), 2013.

[25] J. M. Liu and Z. Q. Zhu, A new sensorless control strategy by high frequency pulsating signal injection into stationary reference frame, In IEEE International Electric Machines and Drives Conference (IEMDC), 2013, pp 505-512.

[26] M. Boussak, Implementation and experimental investigation of sensorless speed control with initial rotor position estimation for interior permanent magnet synchronous motor drive, IEEE Trans. Power Electron. 20 (November (6)) (2005), 1413 – 1422.

[27] H. Kim, K. K. Huh, R. D. Lorenz, and T. M. Jahns, A novel method for initial rotor position estimation for IPM synchronous machine drives, IEEE Trans. Ind. Appl, 40 (October (5)) (2004), 1369 – 1378.

[28] M. Schroedl E. Robeischl, Optimized INFORM-measurement sequence for sensorless PM synchronous motor drives with respect to minimum current distortion. IEEE Trans. Ind. Appl. 40 (April (2)) (2004), 591 – 598.

[29] Y.D. Yoon, S.K. Sul, S. Morimoto and K. Ide, High bandwidth sensorless algorithm for AC machines based on square-wave type voltage injection, IEEE Trans. Ind. Appl, 47 (June (3)) (2011), 1361-1370.

[30] A. Madani, J. P. Barbot, F. Colamartino, C. Marchand, Reduction of torque pulsations by inductance harmonics identification of a permanent-magnet synchronous machine, Proceedings of the 4th IEEE Conference on Control Applications, 1995, pp. 787-792.

[31] G. Foo, M. F. Rahman, Sensorless sliding-mode MTPA control of an IPM synchronous motor drive using a sliding-mode observer and HF signal injection, IEEE Trans. Ind. Electron., 57 (April (4)) (2010), 1270–1278.

[32] G.-D. Andreescu, C. Pitic, F. Blaabjerg, I. Boldea, Combined flux observer with signal injection enhancement for wide speed range sensorless direct torque control of ipmsm drives, IEEE Trans. Energy Convers, 23 (June (2)) (2008), 393 –402.

[33] S. Bolognani, A. Faggion , E. Fornasiero, L. Sgarbossa, Full speed range sensorless IPM motors drives, In: International conference on electrical machines ICEM, Marseille, France; 2012.

[34] H. Rasmussen, Sensorless speed control including zero speed of non salient PM synchronous machines, Bull. Pol. Ac. Tech. 54(3) 2006

[35] H. Dong, C. Zhang, D. Wang, S. Xu, J. Qiu, Dynamic characteristics of gear box with PGT for wind turbine, The 7th International Conference on Sustainable Energy Information Technology, Procedia Computer Science 109C (2017), pp 801–808.

[36] M. Ma, L. Shao, X. Liu, Coordinated control of micro-grid based on distributed moving horizon control, ISA Trans. 76 (2018), 216-225.

[37] D. Zaltni, M. N. Abdelkrim, Robust speed and position observer using HOSM for sensor-less SPMSM control, in Proceedings of the 7th International Multi-Conference on Systems, Signals and Devices (SSD '10), June 2010, pp. 1–6.

[38] A. Chalanga, K. Shyam, L. M. Fridman, B. Bandyopadhyay, J. A. Moreno, Implementation of Super Twisting Control: Super-Twisting and Higher Order Sliding-Mode Observer-Based Approaches, IEEE Trans. Ind. Electron. 63 (6) (2016), 3677-685.

[39] V. Utkin, Discussion Aspects of High Order Sliding Mode Control, IEEE Trans. Automat. Control, 61 (March (3)) (2016), 829 – 833.

[40] S. K. Kommuri, C. K. Veluvolu, M. Defoort, Y. C. Soh3, Higher-Order Sliding Mode Observer for Speed and Position Estimation in PMSM, Hindawi Publishing Corporation Mathematical Problems in Engineering Volume 2014,1-12.

[41] D. Liang, J. Li, R. Qu, Super-Twisting Algorithm Based Sliding Mode Observer for Wide-Speed Range PMSM Sensorless Control Considering VSI Nonlinearity, IEEE International Electric Machines and Drives Conference (IEMDC), 2017.

[42] J. J. Rath1, K. C. Veluvolu, M. Defoort,Y. C. Soh, Higher-order sliding mode observer for estimation of tyre friction in ground vehicles, IET Control Theory Appl. 8 (6) (2014), 399–408.

[43] H. Rasmussen, P. Vadstrup, H. Borsting, Adaptive sensorless field oriented control of PM motors including zero speed, IEEE International Symposium Industrial Electronics, 2004 pp, 1191 – 1196.

[44] H. Chaoui, P. Sicard, Adaptive Fuzzy Logic Control of Permanent Magnet Synchronous Machines With Nonlinear Friction, IEEE Trans. Ind. Electron, 59 (February (2)) (2012), 1123-1133.

[45] N. Bounar, A. Boulkroune, F. Boudjema, M. M'Saad, M. Farza, Adaptive fuzzy vector control for a doubly-fed induction motor, Neurocomputing, 151 (March (Part 2)) (2015), 756-769.

[46] N. Öztürk , E. Çelik, Speed control of permanent magnet synchronous motors using fuzzy controller based on genetic algorithms, Electr. Power Energy Syst. 43 (2012) 889–898.

[47] B. Belabbas, T. Allaoui, M. Tadjine, M. Denai, High Order Sliding Mode Controller Simulation by a Wind Turbine for DFIG Protection against Overcurrent, electrotehcnica, electronica, automatica, 65(4) (2017) 142-147.

[48] S.M. Kazraji, M. B. B. Sharifian, Direct Thrust Force and Flux Control of a PM-Linear Synchronous Motor Using Fuzzy Sliding-Mode Observer, Power Eng And Electr Eng, 13 (1) (2015) 1-9.

***Conflict of Interest**

Conflict of Interest and Authorship Conformation Form

Please check the following as appropriate:

- All authors have participated in (a) conception and design, or analysis and interpretation of the data; (b) drafting the article or revising it critically for important intellectual content; and (c) approval of the final version.
- This manuscript has not been submitted to, nor is under review at, another journal or other publishing venue.
- The authors have no affiliation with any organization with a direct or indirect financial interest in the subject matter discussed in the manuscript
- The following authors have affiliations with organizations with direct or indirect financial interest in the subject matter discussed in the manuscript:

Author's name	Affiliation
Mansouri Mohamed	Laboratory of Energy Engineering and Computer Engineering, IBN Khaldoun University,Tiaret, Algeria.
Hassaine Said	Laboratory of Energy Engineering and Computer Engineering, IBN Khaldoun University, Tiaret, Algeria.
Larbi Mhamed	Laboratory of Energy Engineering and Computer Engineering, IBN Khaldoun University, Tiaret, Algeria.
Bey Mohamed	Laboratory of Energy Engineering and Computer Engineering, IBN Khaldoun University, Tiaret, Algeria.
Allaoui Tayeb	Laboratory of Energy Engineering and Computer Engineering, IBN Khaldoun University, Tiaret, Algeria.
Denai Mouloud	School of Engineering and Technology, University of Hertfordshire, Hatfield, UK
Moudjahed Mohamed	Laboratory of Energy Engineering and Computer Engineering, IBN Khaldoun University, Tiaret, Algeria.